Journal of Solid State Chemistry **168,** 294–305 (2002)
doi:10.1006/jssc.2002.9724

A Structural Investigation of $La_2(GeO_4)O$ and Alkaline-Earth-Doped $La_{9.33}(GeO_4)_6O_2$

P. Berastegui,*,[1] S. Hull,† F. J. García García,* and J. Grins*

*Department of Inorganic Chemistry, Arrhenius Laboratory, Stockholm University, S-106 91 Stockholm, Sweden; and †The ISIS Facility, Rutherford Appleton Laboratory, Didcot, Oxon OX11 0QX, United Kingdom

Received May 10, 2002; in revised form July 3, 2002; accepted July 16, 2002

The structures of the oxyorthogermanate $La_2(GeO_4)O$ and the apatite-structured $La_{9.33}(GeO_4)_6O_2$ have been refined from powder neutron diffraction data. $La_2(GeO_4)O$ crystallizes in a monoclinic unit cell ($P2_1/c$) and is cation stoichiometric in contrast to previous reports. $La_{9.33}(GeO_4)_6O_2$ crystallizes in a hexagonal unit cell ($P6_3/m$) and the powder diffraction data show anisotropic peak broadening that is observed in electron diffraction patterns as incommensurate diffuse spots at *hkq* reciprocal planes (with $q = 1.6-1.7$) and can be attributed to a correlated disorder in the "apatite channels". This compound was doped up to a nominal composition close to $M_2La_8(GeO_4)_6O_2$ with M = Ca, Sr, Ba. The dopant ions preferentially occupy the 4*f* sites as the number of La vacancies decreases. The measured ionic conductivity of $La_{9.33}(GeO_4)_6O_2$ is about 3 orders of magnitude larger than for $La_2(GeO_4)O$ at high temperatures and decreases with increasing dopant content from the highest value of about 0.16 $S\,cm^{-1}$ at 1160 K. © 2002 Elsevier Science (USA)

Key Words: **$La_2(GeO_4)O$; $La_{9.33}(GeO_4)_6O_2$; apatite; powder neutron diffraction; diffuse scattering; Ionic conductivity.**

1. INTRODUCTION

Apatites form an important group of minerals and are known to display a complicated structural chemistry (1). Their composition can be generally described as $M_4M'_6(ZO_4)_6X_2$ with M being a mono-, di- or trivalent cation (e.g., Na^+, Ca^{2+}, La^{3+}), ZO_4 a di-, tri- or tetravalent polyanion (e.g., SO_4^{2-}, PO_4^{3-}, SiO_4^{4-}) and X a mono-, di- or trivalent anion (e.g., F^-, OH^-, O^{2-}, N^{3-}). The apatite structure is thus highly tolerant to cation and anion substitution as well as M and X ion deficiency that can give rise to superstructural ordering or displacive distortions, and the symmetry is usually $P6_3/m$ or one of its subgroups. Of particular interest are the so-called "apatite channels" running along the c-axis at [0,0,z] and [$\frac{1}{3},\frac{2}{3},z$] that are responsible for the main effects on the symmetry and where the X anions and M cations respectively, are located. Compounds with the apatite structure that contain trivalent M cations include a tetravalent ZO_4 group with Z = Ge or Si, in order to maintain the charge balance. An examination of the phase diagrams of the Ln_2O_3–MO_2 systems, where Ln is a lanthanide and M = Si or Ge, reveals the formation of a number of phases depending on the size of the lanthanide ion, temperature and composition (2).

The Y_2O_3–SiO_2 and Ln_2O_3–SiO_2 phase diagrams for Ln = La−Er, all show the presence of three line phases with compositions 1:1, 2:3 and 1:2, i.e., Ln_2SiO_5, $Ln_4Si_3O_{12}$ and $Ln_2Si_2O_7$ (2). The Ln_2SiO_5 phases show only two monoclinic structures, $I2/a$ for the small lanthanides, Ln = Lu−Tb, and $P2_1/c$ for the larger, Ln = Gd−La. In general, $Ln_4Si_3O_{12}$ compounds are reported to be high-temperature phases with hexagonal symmetry. A more detailed study on the Ho_2O_3–SiO_2 system (3) indicated that $Ho_4Si_3O_{12}$ is stable only above 1300°C and formed gradually through the reaction of Ho_2SiO_5 and $Ho_2Si_3O_9$. The $Ho_2Si_3O_9$ compound is reported to display high- and low- temperature monoclinic structures (3), which appears to be reminiscent of the behavior of lanthanide disilicates $Ln_2Si_2O_7$. These in turn are reported to be stable up to 1700–1800°C depending on the lanthanide ion (2). In a study of the Nd_2O_3–SiO_2 system (4), it was reported that the composition $Nd_2Si_2O_7$ decomposed below 1400°C into two phases. One phase has the apatite structure and composition 7:9, i.e., $Nd_{9.33}Si_6O_{26}$, below 1400°C and 2:3, i.e., $Ho_4Si_3O_{12}$, above 1400°C with a small solubility of Nd_2O_3 over the whole temperature range. The second phase was believed to be 1:3 or 1:4 in composition. The $Ln_2Si_2O_7$ phases can be quenched from high-temperature and structural data from neutron diffraction experiments have been recently reported on the high-temperature

[1] To whom correspondence should be addressed. Fax: +46 8 152187. E-mail: pedro@inorg.su.se.

0022-4596/02 $35.00

phases for several compounds [(5) and references therein]. A number of oxyapatite silicates ($P6_3/m$) with the formula $Ln_{9.33}(SiO_4)_6O_2$ and $M_2Ln_8(SiO_4)_6O_2$ compounds have also been reported for the larger lanthanides, while for Ln = Tb–Lu this phase has only been observed as a minor phase (6,7). This structure can be better described as $(Ln^{I}_{3.33}\square_{0.67})Ln^{II}_6(SiO_4)_6O_2$ with the 1/15 Ln cation vacancies located at the Ln^{I} (4*f*) site which is surrounded by nine oxygens and offers a larger space for cation substitution than the Ln^{II} (6*h*) site surrounded by seven oxygens. Substitutions with mono- and divalent alkali ions show that these occupy preferentially the 4*f* site and it has been suggested that oxygen vacancies can be present in the structure if the substitution occurs at the 6*h* site (8).

Information on phase diagrams for the Ln_2O_3–GeO_2 systems is more scarce and show the existence of three phases with compositions 2:1, 1:1 and 1:2 for Ln = Er, Nd and La, and in the Y_2O_3–GeO_2 system. A composition 7:9 is also reported in the La_2O_3–GeO_2 system (9). The Ln_4GeO_8 phases are orthorhombic ($Pm2_1b$) while the Ln_2GeO_5 phases are related to the silicates and show also two monoclinic structures, $I2/a$ for the small lanthanides and $P2_1/c$ for the larger with Ln = Tb–La. The $Ln_2Ge_2O_7$ phases are reported as tetragonal ($P4_12_12$). However, a triclinic structure has also been reported and, to our knowledge, the only apatite-type structures that have been reported in these systems are the $Dy_{9.33}(GeO_4)_6O_2$ (10) and $NaLa_9(GeO_4)_6O_2$ (11) compounds.

Many apatite-structured compounds are known to have good luminescent properties and are also of interest in nuclear waste management (1). Recently, the ionic conducting properties of these materials have been reinvestigated in the silicates and germanates (12,13) as examples of one-dimensional anion conductors. Thus, in a series of samples with composition $Ln_{10}Si_6O_{27}$ with Ln = La–Dy, the activation energy and conductivity were observed to be improved with increasing size of the lanthanide ion and a value for the conductivity of $La_{10}Si_6O_{27}$ at 700°C of $1.08 \times 10^{-2}\,S\,cm^{-1}$ was obtained (12). A recent powder neutron diffraction study of $La_{9.33}Si_6O_{26}$ and $Sr_2La_8Si_6O_{26}$ suggested that these phases crystallize in space group $P\bar{3}$, with Sr occupying both Ln sites and the oxygen ion in the [0,0,z] channels being displaced from the ideal position. The sample stoichiometry is reported as $La_{9.33}Si_6O_{26}$ and a conductivity of $1.2 \times 10^{-4}\,S\,cm^{-1}$ ($E_a = 0.73$ eV) at 700°C was obtained that decreases with Sr doping (13). High values of the conductivity have been also reported for $La_{9.66}Ge_6O_{30-\delta}$ with $\sigma = 0.199\,S\,cm^{-1}$ at 950°C. However, a monoclinic structure was reported for this compound (14).

In order to investigate the stoichiometric, structural and conductivity properties of these compounds in more detail, we have chosen the germanates as an example and present here a structural characterization using X-ray and powder neutron diffraction of pure and Ca-, Sr- and Ba-doped $La_{9.33}(GeO_4)_6O_2$ with the apatite structure and of the oxyorthogermanate $La_2(GeO_4)O$. Electron diffraction experiments have been also carried out in order to study the presence of short- and/or long-range ordered superstructures.

2. EXPERIMENTAL

Samples were prepared by mixing stoichiometric amounts of La_2O_3 (99.9% purity), GeO_2 (99.998%), $BaCO_3$ (>99%) $SrCO_3$ (>99%) and $CaCO_3$ (>99%). La_2O_3 was dried overnight at 1000°C in air before use. These powders were then ground and sintered below 1100°C in air for 24 h. A second sintering was then performed at 1100–1250°C for 2 days and in order to obtain pure La_2GeO_5, the sample was sintered at 1575°C for 6 h. Sample purity was then characterized using X-ray diffraction, and Guinier films were taken using Cu$K\alpha_1$ radiation and analyzed with an automated scanning system.

Two terminal measurements of the ionic conductivity were performed using pelleted samples of about 6 mm diameter and 5 mm length annealed at 1000°C for 6–8 h. The sample was held between two spring-loaded platinum disks inside a boron nitride cell, which is inserted into the hot zone of a horizontal tube furnace. Details of this device can be obtained elsewhere (15). A Solartron S1260 Frequency Response Analyser determined the conventional $Z-Z'$ Bode plot over the frequency range from 10^{-1} to 10^7 Hz. The real component of the sample impedance Z_S was determined using software developed by the authors (15). All measurements were performed under dynamic vacuum of $\sim 10^{-4}$ bar and temperature monitoring was obtained using chromel/alumel thermocouples located ~ 2 mm from the sample pellet.

The diffraction experiments were performed on the Polaris powder diffractometer at the ISIS facility, UK (16) with the samples encapsulated inside thin-walled vanadium cans of 11 mm diameter and 40 mm height. Diffraction data were collected using the backscattering detector bank which covers the scattering angles $135° < \pm 2\theta < 160°$ and provides data over the d-spacing range $0.5 < d(\text{Å}) < 3.2$ with an essentially constant resolution $\Delta d/d \sim 5 \times 10^{-3}$. Rietveld profile refinements using the normalized diffraction data were performed using the program GSAS (17).

Samples for the electron microscopy studies were prepared by grinding the samples under butanol and placing one drop of the suspension onto a holey carbon film supported by a copper grid. These grids were then examined on a JEOL 2000FX transmission electron microscope equipped with a LINK AN10000 energy-dispersive X-ray microanalysis (EDX) system. EDS

analyses were done using a JEOL 820 SEM equipped with a LINK AN10000 EDS microanalysis system.

3. RESULTS AND DISCUSSION

3.1. $La_2(GeO_4)O$

The crystal structure of the oxyorthogermanate La_2GeO_5, also conveniently described as $La_2(GeO_4)O$, is monoclinic (space group $P2_1/c$) and consists of isolated GeO_4 tetrahedra arranged in layers perpendicular to the *a*-axis, see Fig. 1. Results from the Rietveld analysis of the data collected on a sample with La_2GeO_5 stoichiometry at room temperature are presented in Table 1 and the final profile fitting is shown in Fig. 2. The crystallographic data reported for Gd_2GeO_5 were used as the starting model (18). The lanthanum ions are 9 (La(1)) and 7 (La(2)) coordinated with mean La–O distances of 2.622 and 2.505 Å respectively, see Table 2. The La(2) position is located within the layers of GeO_4 tetrahedra while the La(1) ions are above and below the layers with the O(5) ion bridging the two La ions. The observed mean distance in the Ge–O tetrahedra is 1.747 Å. Calculated bond valence sums give values of 2.90 for La(1), 2.92 for La(2) and 4.01 for Ge. A comparison with the structural data reported for La_2GeO_5 (14), Nd_2GeO_5 (19), Eu_2GeO_5 (20), Gd_2GeO_5 and Dy_2GeO_5 (18) shows that the oxygen coordination around the

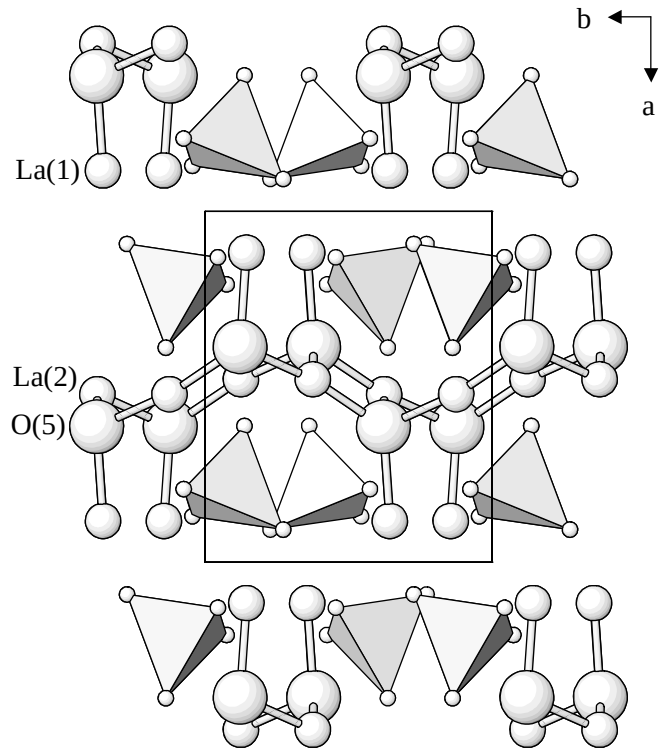

FIG. 1. Crystal structure of $La_2(GeO_4)O$ viewed along the *c*-axis. Small spheres are La ions, larger spheres indicate the position of the O(5) ion. The La(1)–O(5)–La(2) bonds are drawn.

TABLE 1
Refined Atomic Coordinates and Anisotropic Temperature Displacements in La_2GeO_5 at Room Temperature

		x	y	z	U_{eq} (Å^2)	
$P2_1/c$, $a = 9.60405(9)$ Å, $b = 7.46902(7)$ Å, $c = 7.11199(6)$ Å, $\beta = 107.550(1)^\circ$, $V = 486.416(8)$ Å^3						
La(1)	6*h*	0.38289(7)	0.14396(8)	0.58432(9)	0.0053(2)	
La(2)	4*f*	0.02148(6)	0.12451(9)	0.73529(9)	0.0044(2)	
Ge	6*h*	0.29880(6)	0.58817(8)	0.54080(9)	0.0035(2)	
O(1)	6*h*	0.2919(1)	0.0748(1)	0.8573(1)	0.0068(3)	
O(2)	6*h*	0.3695(1)	0.4558(1)	0.7496(1)	0.0102(3)	
O(3)	12*i*	0.4074(1)	0.7723(1)	0.5523(2)	0.0140(4)	
O(4)	2*a*	0.1117(1)	0.6371(1)	0.4917(1)	0.0063(3)	
O(5)	2*a*	0.1140(1)	0.1217(1)	0.4493(1)	0.0061(3)	
	U_{11}	U_{22}	U_{33}	U_{12}	U_{13}	U_{23}
La(1)	0.0055(2)	0.0079(3)	0.0034(2)	0.0007(2)	0.0027(2)	0.0007(2)
La(2)	0.0037(2)	0.0047(2)	0.0048(2)	0.0018(2)	0.0012(2)	0.0003(2)
Ge	0.0033(2)	0.0027(2)	0.0038(2)	0.0002(2)	−0.0001(2)	0.0001(2)
O(1)	0.0077(3)	0.0093(4)	0.0051(3)	0.0012(3)	0.0043(3)	0.0038(3)
O(2)	0.0132(4)	0.0118(4)	0.0035(3)	0.0041(3)	−0.0007(3)	0.0051(3)
O(3)	0.0148(5)	0.0103(4)	0.0199(5)	−0.0106(3)	0.0099(4)	−0.0036(3)
O(4)	0.0035(3)	0.0075(3)	0.0076(4)	0.0021(3)	0.0009(2)	0.0003(3)
O(5)	0.0064(3)	0.0068(4)	0.0055(4)	−0.0001(3)	0.0025(3)	0.0007(3)

$R_{wp} = 0.009$, $R_p = 0.023$, $\chi^2 = 1.60$

$U_{eq} = (\frac{1}{3}) \sum_i \sum_j U_{ij} a_i a_j \, \mathbf{a}_i \cdot \mathbf{a}_j$, anisotropic thermal parameters are of the form $\exp[-2\pi^2(h^2 a^{*2} U_{11} + \ldots + 2hka^* b^* U_{12} + \ldots)]$.
$R_{wp} = \{\sum w_i (I_o - I_c)^2 / \sum w_i I_o^2\}^{1/2}$, $R_p = \sum |I_o - I_c| / \sum I_o$, $\chi^2 = \{\sum w_i (I_o - I_c)^2\} / (N_{obs} - N_{par})$.

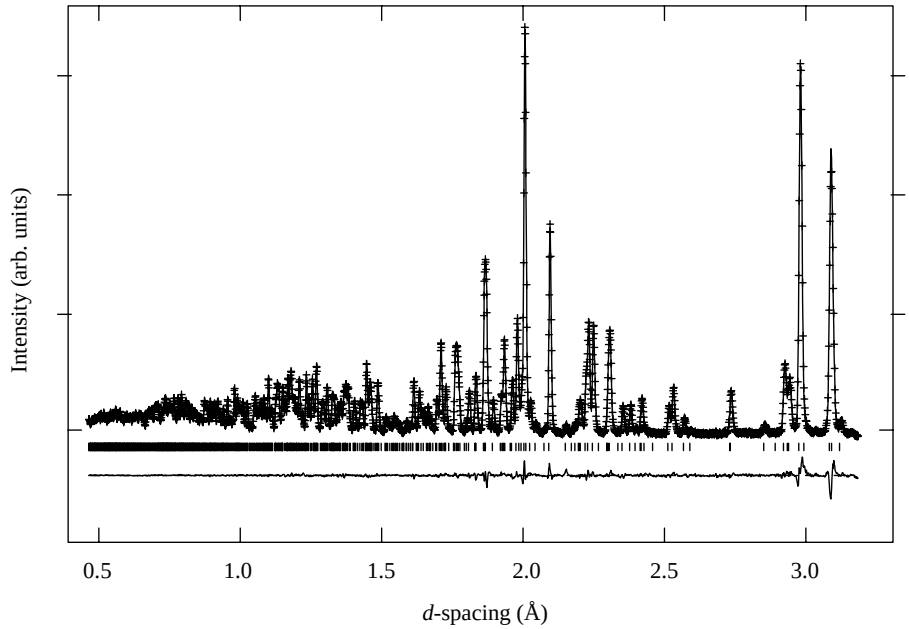

FIG. 2. Least-squares fit to the powder neutron diffraction data collected from La_2GeO_5 at ambient temperature. The dots are the experimental data points and the solid line is the calculated profile. The lower trace shows the difference (measured minus calculated) and the lower tick marks denote the calculated position of the expected reflections.

Ln ions decreases as expected from the decreasing ionic radius, and this is reflected in a decreasing unit cell volume. A more detailed comparison reveals that the GeO_4 tetrahedra rotate to accommodate the larger La ion while the distances between the layers increase. However, such a comparison is only possible with Gd_2GeO_5 as Dy_2GeO_5 crystallizes in a different space group ($I2/a$), the a-axis parameter reported for Eu_2GeO_5 is too large and not in agreement with the powder data reported in the JCPDS (21) and the calculated positions for the oxygen ions in La_2GeO_5 and Nd_2GeO_5 result in very distorted GeO_4 tetrahedra.

In the work by Ishihara *et al.* (14), the authors claimed to have prepared La-deficient samples with composition $La_{2-x}GeO_{5-\delta}$ and with a monoclinic structure for values of $x \leq 0.45$. However, their structural data reveal that the change in the unit cell parameters is not significant although a large decrease would be expected by such an La and O ion deficiency. Furthermore, their structural models reveal very distorted GeO_4 tetrahedra. Attempts to introduce cation vacancies were however carried out by us and samples with composition $La_{2-x}GeO_{5-\delta}$ were prepared for values of $x = 0-0.5$. No reaction was observed below 950°C and the mixtures were thus first heated up to temperatures below 1100°C for at least 12 h in order to avoid loss of GeO_2 due to its high volatility (m.p. = 1115°C). The X-ray diffractograms collected on these samples showed a complex pattern suggesting a unit cell with triclinic symmetry that resembled the calculated pattern for hexagonal apatite. Single-phase samples were obtained for the compositions with $x = 0.45$ (hexagonal apatite-type) and $x = 0$ (monoclinic La_2GeO_5) after a second sintering at 1300°C and 1575°C respectively. Samples with different La contents showed a mixture of hexagonal phase and $La_2Ge_2O_7$ as an impurity or monoclinic La_2GeO_5, depending on the thermal history. Further evidence for the presence of only two line phases, $La_{1.55}GeO_{4.33}$ and La_2GeO_5, within this range of composition was obtained from the cell parameters calculated from the X-ray diffraction patterns. These were observed to be the same within standard deviations for the two phases in all the samples under study. Furthermore, EDS analyses confirmed that the obtained monoclinic samples were of

TABLE 2
Bond Lengths (Å) in La_2GeO_5 at Room Temperature

Atoms	Distance	Atoms	Distance
La(1)–O(1)	2.413(1)	La(2)–O(1)	2.506(1)
La(1)–O(1)	2.632(1)	La(2)–O(4)	2.629(1)
La(1)–O(2)	2.629(1)	La(2)–O(4)	2.483(1)
La(1)–O(2)	2.708(1)	La(2)–O(4)	2.635(1)
La(1)–O(2)	2.460(1)	La(2)–O(5)	2.453(1)
La(1)–O(3)	2.801(1)	La(2)–O(5)	2.402(1)
La(1)–O(3)	2.918(1)	La(2)–O(5)	2.426(1)
La(1)–O(3)	2.564(1)		
La(1)–O(5)	2.474(1)	Ge–O(1)	1.771(1)
		Ge–O(2)	1.742(1)
		Ge–O(3)	1.713(1)
		Ge–O(4)	1.762(1)

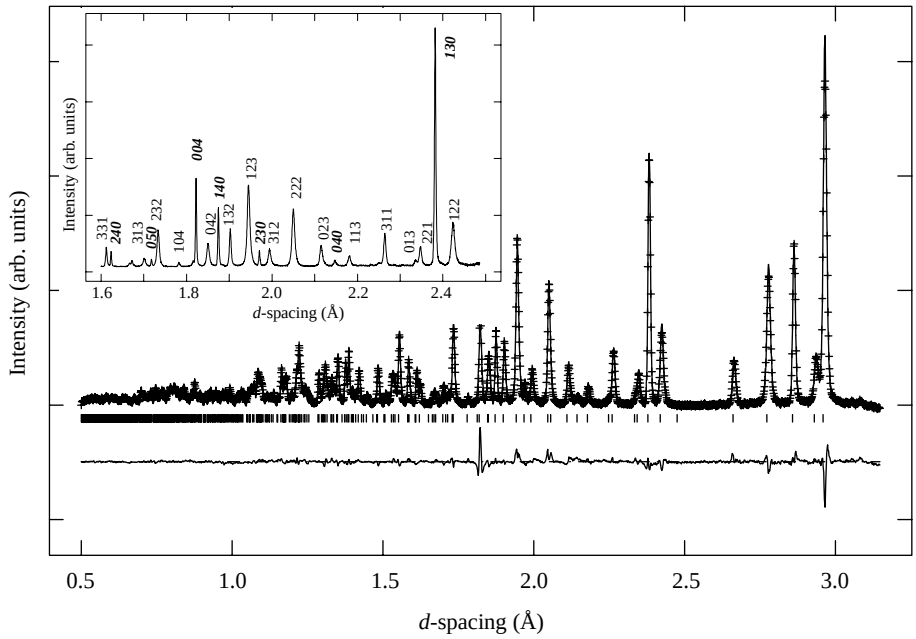

FIG. 3. Least-squares fit to the powder neutron diffraction data collected from $La_{9.33}GeO_{4.33}$ at ambient temperature. The dots are the experimental data points and the solid line is the calculated profile. The lower trace shows the difference (measured minus calculated) and the lower tick marks denote the calculated position of the expected reflections. In the inset is shown part of the high-resolution powder diffractogram collected from $La_{9.33}GeO_{4.33}$ at ambient temperature with the observed sharp reflections indicated in bold.

$La_{2.0(1)}Ge_{1.0(1)}O_5$ stoichiometry. These findings can be explained by GeO_2 loss during the initial sintering and the existence of three line phases in this system for values of $x \leq 1$ ($La_2Ge_2O_7$, $La_{1.55}GeO_{4.33}$ and La_2GeO_5) that have fixed stoichiometry and a new unidentified phase whose structure appears to be a distortion of the hexagonal apatite structure. Similar observations have also been reported in the literature (22).

3.2. $La_{9.33}(GeO_4)_6O_2$

Rietveld analysis on the data collected from a sample with $La_{9.33}(GeO_4)_6O_2$ stoichiometry was performed assuming a fixed oxygen stoichiometry and using the structure reported for $La_{9.33}(SiO_4)_6O_2$ (23) as the starting model. The initial refinements showed a poor agreement of the observed and calculated peak intensities due to an anisotropic broadening of several peaks that was also observed in the X-ray diffraction pattern. A high-resolution powder diffractogram was therefore collected at the HRPD instrument at the ISIS Facility in order to show these broadening effects in more detail. As shown in the inset in Fig. 3, reflections with conditions $hk0$, $00l$ and $0\,k\,0$ are sharp while the remaining reflections show peak broadening. An additional profile parameter was therefore included in the refinement to account for this effect with the anisotropic broadening vector along the c-direction. Refinements in the subgroups of $P6_3/m$ were also tried in an attempt to account for the anisotropy effects but the refinements were not stable and the final refinements in $P6_3/m$ included a scale factor, eight background parameters, four profile coefficients, unit cell parameters and positional and anisotropic temperature factors. The La vacancies were observed to be located only at the 4*f* position and the La occupancies were therefore fixed to the nominal stoichiometry. The refined model is presented in Table 3 and the results of the profile fitting are shown in Fig. 3. It can be seen that the model using anisotropic peak broadening describes the structure well except for the (004) peak at 1.822 Å. An explanation for this effect will be given below.

The apatite-structured $La_{9.33}(GeO_4)_6O_2$ is built by isolated GeO_4 tetrahedra with a mean Ge–O distance of 1.733 Å and mean O–Ge–O angle of 109.4°, and two different polyhedra around the La ions, see Table 4. La(1) is coordinated to seven oxygens at a mean distance of 2.545 Å and La(2) is nine coordinated with a mean La(2)–O distance of 2.656 Å. Calculations of the bond valence sums give values of 2.74 and 2.73 for La(1) and La(2) respectively, an indication that substitution by a larger ion, i.e., alkali or alkaline-earth ions, should be possible. The O(4) ion is located at the central 6_3 axis and fits into the triangular cavities perpendicular to the c-axis that are formed by La(1), and which are surrounded by six parallel columns of La(2) ions, see Fig. 4. The position occupied by the O(4) ion was also refined as a split position in 4*e* with

TABLE 3
Refined Atomic Coordinates and Anisotropic Temperature Displacements in $La_{9.33}(GeO_4)_6O_2$ at Room Temperature

		x	y	z	U_{eq} (Å^2)
$P6_3/m$, $a = 9.9117(1)$ Å, $c = 7.2833(2)$ Å, $V = 619.66(3)$ Å^3					
La(1)	6*h*	0.2305(2)	−0.0107(2)	$\frac{1}{4}$	0.0113(8)
La(2)	4*f*	$\frac{1}{3}$	$\frac{2}{3}$	0.0010(4)	0.0188(9)
Ge	6*h*	0.4011(2)	0.3731(2)	$\frac{1}{4}$	0.0077(7)
O(1)	6*h*	0.3160(4)	0.4893(4)	$\frac{1}{4}$	0.027(2)
O(2)	6*h*	0.6022(3)	0.4764(3)	$\frac{1}{4}$	0.022(1)
O(3)	12*i*	0.3438(3)	0.2502(3)	0.0610(2)	0.041(1)
O(4)	2*a*	0	0	$\frac{1}{4}$	0.048(3)
Occ. La(2) = 0.833					

	U_{11}	U_{22}	U_{33}	U_{12}	U_{13}	U_{23}
La(1)	0.0138(9)	0.0070(7)	0.0080(6)	0.0015(6)	0	0
La(2)	0.0219(8)	0.0219(8)	0.013(1)	0.0109(4)	0	0
Ge	0.0113(8)	0.0042(7)	0.0092(7)	0.0051(6)	0	0
O(1)	0.045(1)	0.042(1)	0.021(1)	0.042(1)	0	0
O(2)	0.015(1)	0.003(1)	0.044(2)	0.002(1)	0	0
O(3)	0.093(2)	0.027(1)	0.0090(5)	0.034(1)	−0.0287(9)	−0.0090(5)
O(4)	0.007(1)	0.007(1)	0.131(7)	0.0035(6)	0	0

$R_{wp} = 0.026$, $R_p = 0.043$, $\chi^2 = 7.96$

$U_{eq} = (\frac{1}{3}) \sum_i \sum_j U_{ij} a_i a_j \, \mathbf{a}_i \cdot \mathbf{a}_j$, anisotropic thermal parameters are of the form $\exp[2\pi^2(h^2 a^{*2} U_{11} + \ldots + 2hka^* b^* U_{12} + \ldots)]$.
$R_{wp} = \{\sum w_i (I_o - I_c)^2 / \sum w_i I_o^2\}^{1/2}$, $R_p = \sum |I_o - I_c| / \sum I_o$, $\chi^2 = \{\sum w_i (I_o - I_c)^2\} / (N_{obs} - N_{par})$.

$z \sim 0.2$ but the refinement did not improve significantly. The coordinates for the ion located at this position are known to be highly dependent on the size of the ion, e.g., in fluorapatite ($z = \frac{1}{4}$), chlorapatite ($z = 0$) and hydroxyapatite ($z = 0.2$), and even modulated structures are known to exist (24). However, the large O(4)–O(4) distance of 3.642 Å along the *c*-axis suggests that the O(4) ion is located at the 4*f* site. The La(1)–O(4) distance of 2.339 Å is shorter than the sum of the ionic radii (25) and has been observed in other rare-earth apatites, indicating the strong polarizing forces of the lanthanide ion on the oxygen not bonded to the tetrahedra (7). Furthermore, the amplitudes of the anisotropic temperature factors are similar to those observed in e.g., the Na-doped structure determined from single crystal data (11) and are largest for the O(1), O(3) and O(4) ions, the latter vibrating along the *c*-axis ($U_{11}/U_{33} = 18.7$) and expected to be the mobile anion. In order to increase the coordination around the La ions, the O(1) ion vibrates toward the La(1) site with the La(1)–O(1) distance being the largest around La(1), 2.786 Å, and the O(3) ion vibrates toward the La(2) ion with an La(2)–O(3) distance of 2.913 Å. In the La(2) channels along the *c*-axis where the vacancies are located, the La(2)–La(2) distances are 3.627 and 3.656 Å, which are much larger than the sum of the ionic radii for La in nine coordination $r_{La}^{3+} = 1.22$ Å (25) and it is likely that the origin of the anisotropic peak broadening arises from a short-range ordering of the La(2) ions along this channel and/or the O(4) ions.

TABLE 4
Bond Lengths (Å) in $La_{9.33}(GeO_4)_6O_2$ at Room Temperature

Atoms	Distance	Atoms	Distance
La(1)–O(1)	2.787(4)	La(2)–O(1)	2.471(3) (×3)
La(1)–O(2)	2.518(3)	La(2)–O(2)	2.582(3) (×3)
La(1)–O(3)	2.634(3) (×2)	La(2)–O(3)	2.914(3) (×3)
La(1)–O(3)	2.450(2) (×2)		
La(1)–O(4)	2.339(2)	Ge–O(1)	1.734(2)
		Ge–O(2)	1.726(3)
		Ge–O(3)	1.735(2) (×2)

In order to investigate this possibility, electron diffraction patterns were collected on an $La_{9.33}(GeO_4)_6O_2$ sample and are shown in Fig. 5. In Figs. 5a, 5c and 5h three electron diffraction patterns (EDP) down [001], ⟨100⟩ and ⟨110⟩ respectively are presented. The pattern shown in Fig. 5b was recorded after tilting the pattern presented in Fig. 5a while keeping excited one of the $\langle 1\bar{1}00 \rangle^*$. In this pattern, highly structured diffuse scattering that defines faint circles between the rows of reflections of the basic hexagonal structure can be observed. In Figs. 5d and 5e the resulting patterns after tilting the crystal by a few degrees out of the exact $\langle \bar{1}10 \rangle$ zone axis condition while keeping the main perpendicular directions are shown. The same experiments carried out down ⟨110⟩ are presented in Figs. 5f and 5g. Note that Figs. 5d–5g were recorded down reciprocal directions near the corresponding perfect zone axis condition but the pattern in Fig. 5b was reached after tilting a considerably larger angle. Magnified details of the

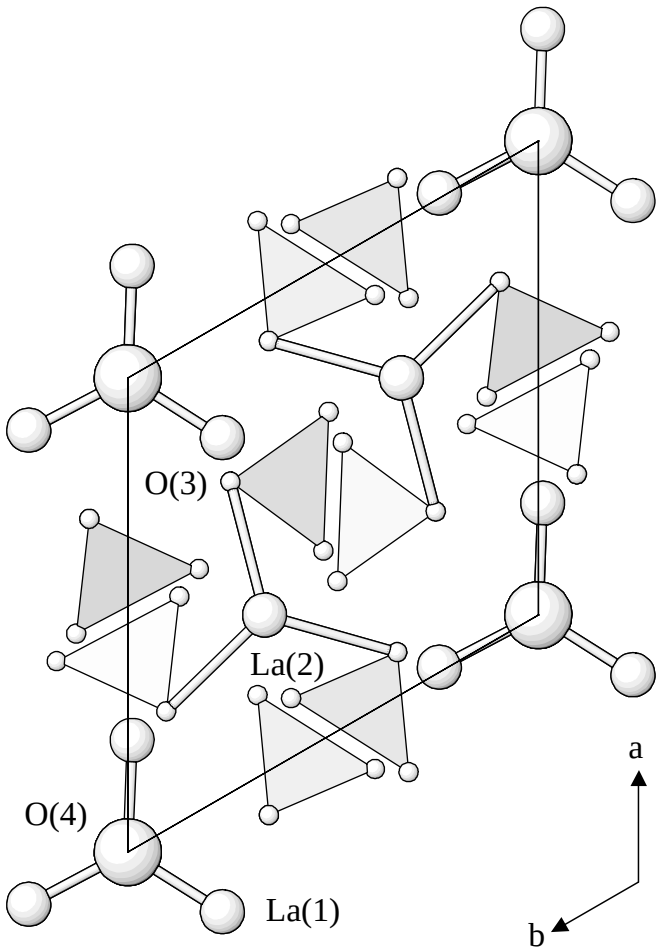

FIG. 4. Crystal structure of $La_{9.33}(GeO_4)O_2$ viewed along the *c*-axis. Small spheres are La ions, larger spheres indicate the position of the O(4) ion. The La(2)–O(4) and La(1)–O(3) bonds are drawn to indicate the channels at [0,0,*z*] and $[\frac{1}{3},\frac{2}{3},z]$.

diffuse intensity distribution can be seen in the insets in Figs. 5e and 5g. Furthermore, satellite reflections can also be distinguished where the diffuse scattering seems to condense, which are marked in Figs. 5d–f. Thus, these electron diffraction experiments show the presence of a highly structured diffuse intensity distribution in addition to the reciprocal lattice associated with the basic hexagonal apatite structure. There are several cases described in the literature where non-stoichiometry at the *X* position has been proposed to induce displacive distortions in the parent hexagonal structure. Such distortions cause a modulation of the structure, and single crystal refinements have shown that a "chimney-ladder" description is highly convenient (26). Thus, atoms sited at the channels at the [0,0,*z*] position move slightly along the hexagonal axis generating a different periodicity to that of the host structure. As a result the so-called "host structure" remains basically unmodulated and the rods of *X* atoms show a distortion from the basic apatite structure (27). Disorder within the channels at $[\frac{1}{3},\frac{2}{3},z]$ should generate the same kind of intra- and inter-rod interactions, giving rise to similar effects in the electron diffraction experiments.

The diffuse intensity distribution seen in Fig. 5b together with the satellites observed when the crystals are slightly tilted off down $\langle \bar{1}10 \rangle^*$ and $\langle 110 \rangle^*$ confirms that all the observed diffuse intensity lies in the *hkq* reciprocal planes, with $q \sim 1.6-1.7\ c^*$. Such reciprocal space details resemble those reported in Ref. (26) where a complete analysis of possible real space distortions and their effects in reciprocal space has been performed using computer modeling, including the study of possible disorder in the channels at

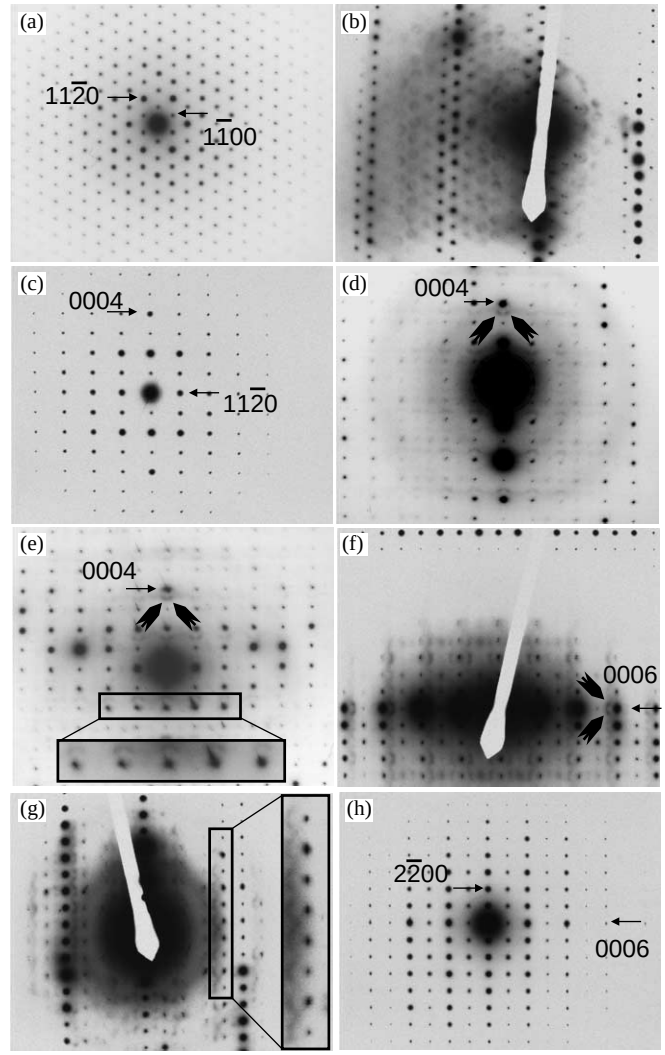

FIG. 5. Typical zone axis electron diffraction patterns taken on $La_{9.33}(GeO_4)_6O_2$ sample are shown down: (a) [001], (c) $\langle 100 \rangle$ and h) $\langle 110 \rangle$. In (b) is shown the pattern recorded after tilting off the [001] pattern presented in a). In (d) and (e) the resulting patterns after tilting the crystal a few degrees out of the exact $\langle \bar{1}10 \rangle$ zone axis condition while keeping the main perpendicular directions are shown. The corresponding tilting experiments down $\langle 110 \rangle$ are presented in (f) and (g).

$[\frac{1}{3},\frac{2}{3},z]$ along with possible inter-rods interactions (i.e., correlation within the (001) planes). In the present case, a similar study is needed in order to explain the observed details in the powder neutron data and in the electron diffraction experiments. However, such studies are outside the scope of this article and here we only point out a few important observations in relation to those previously reported (26). Diffuse intensity was not observed when viewed down the main reciprocal directions [001], $\langle \bar{1}10 \rangle$ and $\langle 110 \rangle$, which means that the structure corresponds exactly to the average structure when looking down those directions. Moreover, diffuse intensity at $hk2q$ was not observed either, which suggests that the distortions of the basic structure are small. The analysis of the powder neutron diffraction data showed highly anisotropic displacement parameters for the O ions at the $(0,0,\frac{1}{4})$ positions and vacancy disorder within the La columns at $[\frac{1}{3},\frac{2}{3},z]$. The observed peak broadening should be then directly related to the observed diffuse scattering in the EDP as these effects were not observed in the doped compound. The diffuse scattering is therefore likely to be due to a small disorder of O and La ions sited at both channels and can be observed as not well-defined spots apart from the set of strong reflections from the basic structure. Furthermore, there is probably also a correlation between both channels as suggested from the condensation into spots. If there were no correlations between the channels, planes of diffuse scattering would be observed instead. However, the Rietveld analysis of the neutron powder diffraction data cannot account for this short-range ordering and this explains the difficulties in obtaining a better fit to the neutron data from the model used in the refinements.

3.3. Doped $La_{9.33}(GeO_4)_6O_2$

Examples of doped apatite-structured $Ln_{9.33}(ZO_4)_6O_2$ where Z = Ge or Si are known and reflect the tolerance for doping with ions of different size and valence at the Ln^{3+} sites in this structure. The conductivity and structure of Li-doped $Ln_{10}(SiO_4)_6O_2$ compounds (28) and the structure of cation stoichiometric $Ca_2La_8(SiO_4)_6O_2$ (29), $Ca_2Nd_8(SiO_4)_6O_2$ (8) and $NaY_9(SiO_4)_6O_2$ (30) among the silicates and also of $NaLa_9(GeO_4)_6O_2$ (11) have been reported. In all these cases, the dopant ion is shown to occupy preferentially the $4f$ site and a short La(1)–O(4) distance smaller than the sum of ionic radii (2.44 Å) is observed, indicating a strong polarization of the O ion in the 6_3 channels (7). In the case of $Ca_{2+x}Nd_{8-x}(SiO_4)_6O_{2-0.5x}$, a solubility limit of $x \leq 1.0$ at 1250°C has been reported (8), which would imply an increasing amount of Ca at the $6h$ site and an occupation of $\frac{3}{4}$ at the O(4) site. Studies have been therefore carried out in a series of $M_{6x}La_{9.33-4x}(GeO_4)_6O_2$ compounds with M = Ca, Sr and Ba in order to investigate the solubility limits and the effects of the size of the dopant ion on the structure. The samples were sintered at 1250°C and the solubility limits were determined by examination of the unit cell parameters and phase purity. It was observed that for compositions higher than $x = 0.33$, which would correspond to a stoichiometry of $Ca_2La_8(GeO_4)_6O_2$, alkaline-earth germanates with low melting points formed and those samples were thus sintered at 1100°C. When doping with the smaller Ca ion ($r_{La}3+ = 1.22$, $r_{Ca}2+ = 1.18$ Å) (25), a solubility limit was clearly observed at about $x = 0.3$, see Fig. 6. Above this composition there is no further decrease in unit cell volume and $CaGe_2O_5$ is observed as an impurity. When doping with the larger Sr ion ($r_{Sr}2+ = 1.31$ Å), a slight increase in the unit cell volume is observed up to about $x = 0.3$. At higher Sr contents, $SrGeO_3$ is observed as an impurity and there is no change in the unit cell volume. Ba doping causes a large increase in the unit cell volume and a solubility limit of $x = 0.3$ is also observed in this case with Ba_2GeO_4 observed at higher Ba contents.

Powder neutron diffraction data were collected on the Ca and Sr series of samples and during the Rietveld refinements, the total Ca and Sr content was fixed to the nominal value that had been confirmed by EDS analyses. The refinement of the La(2) site occupancy resulted in a content close within e.s.d.'s to the one required to maintain charge balance and was therefore also fixed to the nominal value. The refined atomic positions are presented in Tables 5 and 6. The assumption that the small cavities at the $6h$ site with a very short La(1)–O(4) distance are unfavorable for cations with large radius and/or low charge (31) is demonstrated here by the small occupancy of Sr and Ca observed at this site and the La/M(1)–O(4) distance, that decreases slightly with Ca doping but remains constant

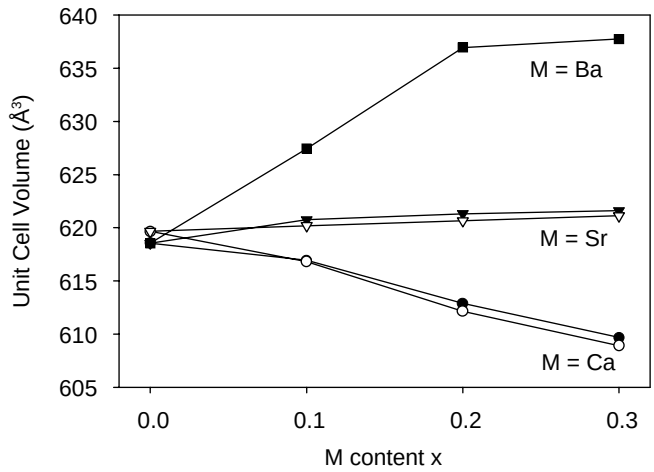

FIG. 6. Changes in the unit cell volume as a function of dopant content in $M_{6x}La_{9.33-4x}(GeO_4)_6O_2$ compounds. Closed symbols are from X-ray measurements and open symbols from neutron diffraction data. Error bars are smaller than the symbols.

TABLE 5
Refined Atomic Coordinates and Equivalent Temperature Displacements in $Ca_{6x}La_{9.33-4x}(GeO_4)_6O_2$ at Room Temperature

		x	y	z	U_{eq} (Å^2)
$Ca_{0.6}La_{8.933}(GeO_4)_6O_2$ ($P6_3/m$, $a = 9.90087(8)$ Å, $c = 7.2657(1)$ Å, $V = 616.81(1)$ Å^3)					
La/Ca(1)	6*h*	0.2306(2)	−0.0108(2)	$\frac{1}{4}$	0.0097(5)
La/Ca(2)	4*f*	$\frac{1}{3}$	$\frac{2}{3}$	0.0001(3)	0.0152(7)
Ge	6*h*	0.4016(1)	0.3737(1)	$\frac{1}{4}$	0.0065(5)
O(1)	6*h*	0.3173(3)	0.4910(2)	$\frac{1}{4}$	0.021(1)
O(2)	6*h*	0.6038(2)	0.4764(2)	$\frac{1}{4}$	0.022(1)
O(3)	12*i*	0.3443(2)	0.2513(2)	0.0610(2)	0.040(1)
O(4)	2*a*	0	0	$\frac{1}{4}$	0.039(2)
Occ. La/Ca(1) = 0.977(9)/0.023(9)					
Occ. La/Ca(2) = 0.77(1)/0.12(1)					
$R_{wp} = 0.022$, $R_p = 0.033$, $\chi^2 = 4.93$					
$Ca_{1.2}La_{8.533}(GeO_4)_6O_{2-\delta}$ ($P6_3/m$), $a = 9.87796(6)$ Å, $c = 7.24430(8)$ Å, $V = 612.155(8)$ Å^3)					
La/Ca(1)	6*h*	0.2301(1)	−0.0114(1)	$\frac{1}{4}$	0.0077(4)
La/Ca(2)	4*f*	$\frac{1}{3}$	$\frac{2}{3}$	−0.0004(2)	0.0128(5)
Ge	6*h*	0.4025(1)	0.3744(1)	$\frac{1}{4}$	0.0055(4)
O(1)	6*h*	0.3180(2)	0.4920(2)	$\frac{1}{4}$	0.0164(8)
O(2)	6*h*	0.6050(2)	0.4758(2)	$\frac{1}{4}$	0.0218(8)
O(3)	12*i*	0.3430(2)	0.2508(2)	0.0610(1)	0.0379(8)
O(4)	2*a*	0	0	$\frac{1}{4}$	0.031(1)
Occ. La/Ca(1) = 0.987(7)/0.013(7)					
Occ. La/Ca(2) = 0.65(1)/0.28(1)					
$R_{wp} = 0.018$, $R_p = 0.030$, $\chi^2 = 3.57$					
$Ca_{1.8}La_{8.133}(GeO_4)_6O_{2-\delta}$ ($P6_3/m$, $a = 9.86351(5)$ Å, , $c = 7.22692(6)$ Å, $V = 608.901(7)$ Å^3)					
La/Ca(1)	6*h*	0.2298(1)	−0.0119(1)	$\frac{1}{4}$	0.0067(3)
La/Ca(2)	4*f*	$\frac{1}{3}$	$\frac{2}{3}$	−0.0003(2)	0.0106(4)
Ge	6*h*	0.4031(1)	0.3750(1)	$\frac{1}{4}$	0.0048(3)
O(1)	6*h*	0.3186(1)	0.4929(1)	$\frac{1}{4}$	0.0129(6)
O(2)	6*h*	0.6061(1)	0.4753(1)	$\frac{1}{4}$	0.0208(6)
O(3)	12*i*	0.3414(1)	0.2501(1)	0.0610(1)	0.0358(6)
O(4)	2*a*	0	0	$\frac{1}{4}$	0.0254(9)
Occ. La/Ca(1) = 0.993(6)/0.007(6)					
Occ. La/Ca(2) = 0.543(9)/0.440(9)					
$R_{wp} = 0.017$, $R_p = 0.027$, $\chi^2 = 3.39$					

$U_{eq} = (\frac{1}{3})\sum_i \sum_j U_{ij} a_i a_j \, \mathbf{a}_i \cdot \mathbf{a}_j$.
$R_{wp} = \{\sum w_i (I_o - I_c)^2 / \sum w_i I_o^2\}^{1/2}$, $R_p = \sum |I_o - I_c| / \sum I_o$, $\chi^2 = \{\sum w_i (I_o - I_c)^2\} / (N_{obs} - N_{par})$.

with Sr doping. It is therefore expected that Ba occupies only the 4*f* sites causing the rapid increase in the unit cell volume. As the dopant content increases, the number of La vacancies decreases at the 4*f* site and the dopant ions are transferred from the 6*h* to the 4*f* site until a composition $M_2La_8(GeO_4)_6O_2$ is reached.

It appears that the Sr dopant content can be further increased by a slower decrease of the amount of Sr at the 6*h* sites while maintaining charge balance. The mean Ge–O distances remain constant with doping, while the La–O distances reflect the effect of doping with ions of different size at the La(2) site. Thus, with Ca doping, the mean La/*M*(1)–O distance decreases from 2.545 to 2.534 Å at $x = 0.3$ and the mean La/*M*(2)–O distance decreases slightly more due to the larger Ca doping at this site from 2.656 to 2.632 Å at $x = 0.3$. With Sr doping, the mean La(1)–O distance decreases to 2.534 Å while the La(2)–O distance increases to 2.669 Å due to the larger size of the Sr ion. These changes are analogous to the observed changes in unit cell parameters and imply that the La(1) site is not affected by the filling of vacancies occurring at the La(2) site.

Electron diffraction experiments carried out on a Ca-doped sample did not show any additional diffracted intensity apart from the strong Bragg reflections defining the reciprocal lattice of the basic hexagonal structure. Furthermore, the powder neutron diffraction data did not show anisotropic peak broadening as observed in the undoped sample. Hence, the assumption made above concerning the origins of both effects is demonstrated, as the number of La vacancies that cause the modulation in the pure compound is less in the doped case and the dopant ion can be considered to stabilize the structure.

TABLE 6
Refined Atomic Coordinates and Equivalent Temperature Displacements in $Sr_{6x}La_{9.33-4x}(GeO_4)_6O_{2-\delta}$ at Room Temperature

		x	y	z	U_{eq} (Å^2)
$Sr_{0.6}La_{8.933}(GeO_4)_6O_2$ ($P6_3/m$, $a = 9.90748(7)$ Å, $c = 7.29578(9)$ Å, $V = 620.20(1)$ Å^3)					
La/Sr(1)	6*h*	0.2304(1)	−0.0105(2)	$\frac{1}{4}$	0.0089(5)
La/Sr(2)	4*f*	$\frac{1}{3}$	$\frac{2}{3}$	0.0012(3)	0.0144(6)
Ge	6*h*	0.4005(1)	0.3727(1)	$\frac{1}{4}$	0.0063(5)
O(1)	6*h*	0.3144(2)	0.4881(2)	$\frac{1}{4}$	0.021(1)
O(2)	6*h*	0.6026(2)	0.4766(2)	$\frac{1}{4}$	0.0179(8)
O(3)	12*i*	0.3431(2)	0.2494(2)	0.0612(2)	0.0320(8)
O(4)	2*a*	0	0	$\frac{1}{4}$	0.030(1)
Occ. La/Sr(1) = 0.95(2)/0.05(2)					
Occ. La/Sr(2) = 0.80(3)/0.08(3)					
$R_{wp} = 0.021$, $R_p = 0.034$, $\chi^2 = 4.90$					
$Sr_{1.2}La_{8.533}(GeO_4)_6O_{2-\delta}$, ($P6_3/m$, $a = 9.90298(5)$ Å, $c = 7.30786(6)$ Å, $V = 620.659(7)$ Å^3)					
La/Sr(1)	6*h*	0.2301(1)	−0.0106(1)	$\frac{1}{4}$	0.0070(3)
La/Sr(2)	4*f*	$\frac{1}{3}$	$\frac{2}{3}$	0.0011(2)	0.0108(4)
Ge	6*h*	0.4001(1)	0.3722(1)	$\frac{1}{4}$	0.0054(4)
O(1)	6*h*	0.3129(2)	0.4870(2)	$\frac{1}{4}$	0.0154(7)
O(2)	6*h*	0.6029(2)	0.4766(2)	$\frac{1}{4}$	0.0139(6)
O(3)	12*i*	0.3413(1)	0.2480(1)	0.0616(1)	0.0240(5)
O(4)	2*a*	0	0	$\frac{1}{4}$	0.0206(8)
Occ. La/Sr(1) = 0.96(2)/0.04(2)					
Occ. La/Sr(2) = 0.69(2)/0.25(2)					
$R_{wp} = 0.017$, $R_p = 0.028$, $\chi^2 = 3.00$					
$Sr_{1.8}La_{8.133}(GeO_4)_6O_{2-\delta}$ ($P6_3/m$, $a = 9.90114(4)$ Å, $c = 7.31609(5)$ Å, $V = 621.126(5)$ Å^3)					
La/Sr(1)	6*h*	0.2303(1)	−0.0105(1)	$\frac{1}{4}$	0.0058(2)
La/Sr(2)	4*f*	$\frac{1}{3}$	$\frac{2}{3}$	0.0006(1)	0.0088(3)
Ge	6*h*	0.3998(1)	0.3720(1)	$\frac{1}{4}$	0.0047(2)
O(1)	6*h*	0.3123(1)	0.4863(1)	$\frac{1}{4}$	0.0123(4)
O(2)	6*h*	0.6027(1)	0.4763(1)	$\frac{1}{4}$	0.0113(4)
O(3)	12*i*	0.3400(1)	0.2470(1)	0.0618(1)	0.0189(3)
O(4)	2*a*	0	0	$\frac{1}{4}$	0.0144(5)
Occ. La/Sr(1) = 0.97(1)/0.03(1)					
Occ. La/Sr(2) = 0.57(2)/0.41(2)					
$R_{wp} = 0.013$, $R_p = 0.024$, $\chi^2 = 1.87$					

$U_{eq} = (\frac{1}{3})\sum_i \sum_j U_{ij} a_i a_j \, \mathbf{a}_i \cdot \mathbf{a}_j$.
$R_{wp} = \{\sum w_i (I_o - I_c)^2 / \sum w_i I_o^2\}^{1/2}$, $R_p = \sum |I_o - I_c| / \sum I_o$, $\chi^2 = \{\sum w_i (I_o - I_c)^2\} / (N_{obs} - N_{par})$.

3.4. Conductivity Measurements

Measurements of the ionic conductivity show a significant difference between monoclinic $La_2(GeO_4)O$ and hexagonal $La_{9.33}(GeO_4)_6O_2$ as seen in Fig. 7. The one-dimensional channels in the apatite structure seem therefore to be the pathways for the anion diffusion. A change in the slope of the conductivity curve can be observed at 1000 K in the undoped compound and at lower temperatures in the doped compounds. At the same time, the conductivity in the high-temperature region decreases with dopant content, i.e., as the cation vacancy content decreases and no significant difference is observed between Sr and Ca doping, see Figs. 7 and 8. The change in the slope of the conductivity curve at high temperature is likely to be due to a rearrangement of the La vacancies on the two available sites, that decrease in number as the composition $M_2La_8(GeO_4)_6O_2$ is reached. This is expected to influence the oxygen channels and suggests that the conductivity can be optimized by varying the number of cation vacancies (32). The highest value for the conductivity is 0.16 S cm^{-1} at 1160 K for $Sr_{0.6}La_{8.933}(GeO_4)_6O_2$ and the value at 975 K agrees very well with the conductivity obtained for the related $La_{10}Si_6O_{27}$ (11) of about 10^{-2} S cm^{-1}.

4. CONCLUSIONS

The La_2O_3–GeO_2 system has been studied by a combination of X-ray, neutron and electron diffraction techniques and displays four phases at La contents above 50%, La_2GeO_5, $La_{1.55}GeO_{4.33}$, $La_2Ge_2O_7$ and a new phase with possible triclinic symmetry and a distorted apatite-like

structure. The structure of the monoclinic oxyorthogermanate $La_2(GeO_4)O$ is related to the $Gd_2(GeO_4)O$ compound with a layered structure and is found to be cation stoichiometric in contrast to the results reported by Ishihara *et al*. (14), who report an La-deficient monoclinic structure in $La_{2-x}GeO_{5-\delta}$ for values of $x \leq 0.45$. The apatite-like structured $La_{9.33}(GeO_4)_6O_2$ contains cation vacancies at the $[\frac{1}{3},\frac{2}{3},z]$ columns that cause a modulation along the *c*-axis observed from electron diffraction measurements. The diffuse scattering is also likely to be due to a small disorder of O ions sited at $(0,0,\frac{1}{4})$, as ill-defined spots apart from the set of strong reflections from the basic structure can be observed in the EDP. There is probably also a correlation between both channels and it is likely that the same effect should be observed in other rare-earth apatites with cation vacancies. This structure can be doped with M^+ and M^{2+} cations at the La sites. In the latter case, a solubility limit of $M_2La_8(GeO_4)_6O_2$ at 1100°C is observed as the cation vacancies are filled with M^{2+} ions. However, it is possible that the solubility is higher at higher temperatures. A small occupancy of M^{2+} ions at the fully occupied 6*h* site is observed to decrease with increasing dopant content, while the La–O distances reflect the doping effects of the M^{2+} ions of different size. The ionic conductivity is larger in the apatite structured $La_{9.33}(GeO_4)_6O_2$, with one-dimensional channels available for oxygen ion diffusion, than in $La_2(GeO_4)O$. A change in slope of the conductivity curve at high temperatures suggests a redistribution of the La vacancies and only a small increase in conductivity is observed at low dopant contents.

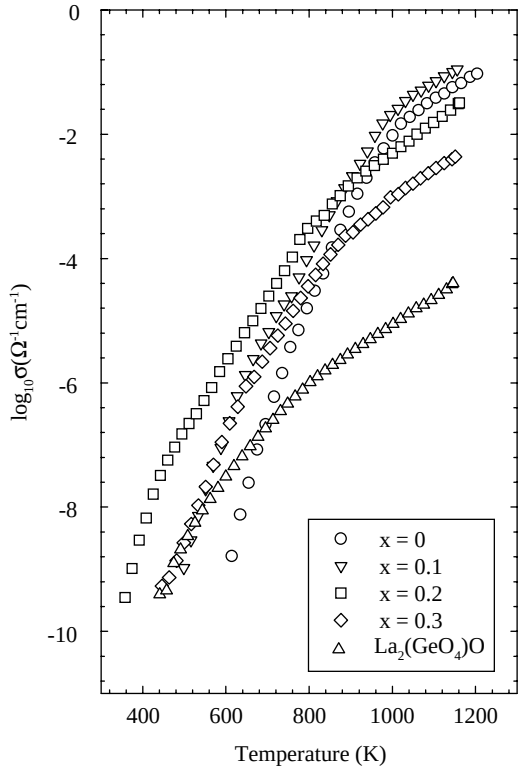

FIG. 7. Temperature dependence of the total conductivity in the $Sr_{6x}La_{9.33-4x}(GeO_4)_6O_2$ series and $La_2(GeO_4)O$.

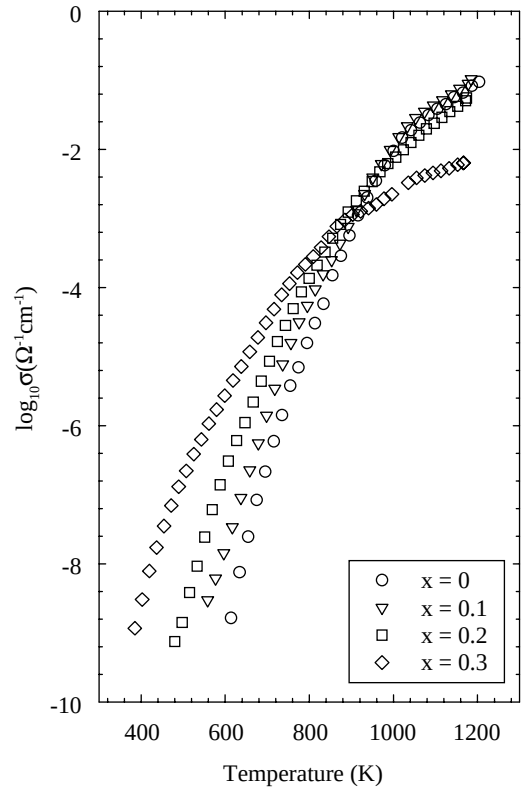

FIG. 8. Temperature dependence of the total conductivity in the $Ca_{6x}La_{9.33-4x}(GeO_4)_6O_2$ series.

ACKNOWLEDGMENTS

The Swedish Research Council is acknowledged for financial support.

REFERENCES

1. D. McConnell, "Apatite." Springer-Verlag, Wien New York, 1973.
2. "Phase Diagrams for Ceramists." NIST, American Ceramic Society.
3. M. Montorsi, *J. Less-Common Met*. **84,** 25 (1982).
4. N. A. Toporov and M. V. Kougiya, *Inorg. Mater*. **7,** 1082 (1971). [Engl. Transl.]
5. A. N. Christensen, *Z. Kristallogr*. **209,** 7 (1994).
6. Yu. I. Smolin and Yu. F. Shepelev, *Acta Crystallogr. B* **26,** 484 (1970).
7. J. Felsche, *J. Solid State Chem*. **5,** 266 (1972).
8. J. A. Fahey, W. J. Weber, and F. J. Rotella, *J. Solid State Chem*. **60,** 145 (1985).
9. A. Bondar, *Inorg. Mater*. **15,** 793 (1979). [Engl. Transl.]

10. E. L. Belokoneva, T. L. Petrova, M. A. Simonov, and N. V. Belov, *Kristallografiya* **17,** 490 (1972).
11. M. Takahashi, K. Uematsu, Z.-G. Ye, and M. Sato, *J. Solid State Chem.* **139,** 304 (1998).
12. S. Nakayama and M. Sakamoto, *J. Eur. Ceram. Soc.* **18,** 1413 (1998).
13. J. E. H. Sansom, D. Richings, and P. R. Slater, *Solid State Ionics* **139,** 205 (2001).
14. T. Ishihara, H. Arikawa, T. Akbay, H. Nishiguchi, and Y. Takita, *J. Am. Chem. Soc.* **123,** 203 (2001).
15. N. J. G. Gardner, S. Hull, D. A. Keen, and P. Berastegui, Rutherford Appleton Laboratory Report, RAL-TR-1998-032, 1998.
16. S. Hull, R. I. Smith, W. I. F. David, A. C. Hannon, J. Mayers, and R. Cywinski, *Physica B* **180–181,** 1000 (1992).
17. A. C. Larson and R. B. Von Dreele, "General Structural Analysis System (GSAS)." Los Alamos National Laboratory, Los Alamos, NM, 1994.
18. L. Brixner, J. Calabrese, and H. Y. Chen, *J. Less-Common Met.* **110,** 397 (1985).
19. A. G. Vigdorchik, L. N. Demyanets, and Yu. A. Malinovskii, *Kristallografiya* **32,** 1381 (1986).
20. K. Kato, M. Sekita, and S. Kimura, *Acta Crystallogr. B* **35,** 2201 (1979).
21. JCPDS-International Centre for Diffraction Data (1997).
22. J. E. H. Sansom, L. Hildebrandt, and P. R. Salter, *Ionics* **8,** 155 (2002).
23. E. A. Kuzmin and A. N. V. Belov, *Dok. Akad. Nauk* **165,** 88 (1965).
24. K. Sudarsanan, R. A. Young, and A. J. C. Wilson, *Acta Crystallogr. B* **33,** 3136 (1977).
25. R. D. Shannon and C. T. Prewitt, *Acta Crystallogr. B* **25,** 925 (1969).
26. A. G. Chirsty, P. Alberius-Henning, and S. Lidin, *J. Solid State Chem.* **156,** 88 (2001).
27. P. Alberius-Henning, M. Moustiakimov, and S. Lidin, *J. Solid State Chem.* **150,** 154 (2000).
28. M. Sato, Y. Kono, H. Ueda, K. Uematsu, and K. Toda, *Solid State Ionics* **83,** 249 (1996).
29. R. P. Gunawardane, R. A. Howie, and F. P. Glasser, *Acta Crystallogr. B* **38,** 1564 (1982).
30. L. W. Schroeder and M. Mathew, *J. Solid State Chem.* **26,** 383 (1978).
31. G. Blasse, *J. Solid State Chem.* **14,** 181 (1975).
32. E. J. Abram, D. C. Sinclair, and A. R. West, *J. Mater. Chem.* **11,** 1978 (2001).